



Constructing 2D graphitic carbon nitride nanosheets/layered MoS₂/graphene ternary nanojunction with enhanced photocatalytic activity

Hongwei Tian*, Ming Liu, Weitao Zheng*

Key Laboratory of Automobile Materials of MOE and Department of Materials Science, Jilin University, Changchun, 130012, China



ARTICLE INFO

Keywords:

2D heterostructure
G-C₃N₄ nanosheets
MoS₂/graphene cocatalyst
Photocatalysis
Visible light

ABSTRACT

Two-dimensional (2D) nanosheets materials have attracted extensive attention because of their promising practical application and theoretical values. In order to enhance the photocatalytic activity of bulk C₃N₄, we designed a 2D fabrication in which g-C₃N₄ nanosheets was in the middle of MoS₂/graphene layered structure. Here, we report an effective strategy to synthesize ternary g-C₃N₄/MoS₂/graphene nanocomposite photocatalyst via an in-situ adsorption method, which exhibits superior photocatalytic activity owing to enhanced charge carrier separation via well-contacted interface and fast charge transfer pathway. This work indicates a new insight into the design of such 2D heterostructure and a promising cocatalyst strategy for designing a more efficient g-C₃N₄-based semiconductor photocatalyst toward degradation of organic pollutants.

1. Introduction

2D nanosheets materials, made of few atomic layers, have attracted tremendous attention owing to their unique properties and potential applications in the areas of electronics, sensors, catalysts and energy storage devices [1–4]. As for photocatalysts, nanosheets are extremely advantageous for promoting photocatalysis efficiency [5–7]. The apparent advantages associated with nanosheets include large specific surface area for providing abundant reactive sites and short bulk diffusion length for reducing the recombination probability of photo-excited charge carriers. In particular, recent investigations of graphene, a 2D aromatic monolayer of carbon atoms, have demonstrated exceptional physical properties, including ultrahigh electron mobility, ballistic transport and other properties [8,9]. To date, great efforts have been undertaken to synthesize atomic-thick nanosheets of both the intrinsically layered structural and nonlayered structural materials and explore their abundant properties, such as nitrides, oxides, and sulfides [10–12]. For instance, C₃N₄, MoS₂ and WS₂ nanosheets have been fabricated via the exfoliation of their bulk layered counterparts. [13–15]

Graphitic carbon nitride (g-C₃N₄) with a 2D layered structure is a graphite-like layered material in fact, where there are tris-triazine units connected with planar amino groups in each layer and weak van der waals force between layers [16]. Distinct from bulk C₃N₄, g-C₃N₄ nanosheets may possess a much higher surface area with abundant surface active sites, a larger bandgap because of the quantum size effect and improved electron transport ability along the in-plane direction [17].

As a metal-free semiconductor, g-C₃N₄ has received considerable attention owing to its high thermal and chemical stability, non-toxicity and fascinating photocatalytic performances under visible-light to be widely used in photodegradation [18–20], photocatalytic water splitting [21,22], activation of carbon dioxide [23], removal of nitric oxide [24], decomposition of formaldehyde [25] and energy-related hot topics to other new emerging fields, such as sensing, imaging and therapy [26–28]. However, the photocatalytic performance of g-C₃N₄ is limited by slow electron transfer and fast charge recombination. To increase the activity of g-C₃N₄ photocatalyst, many strategies such as introducing heteroatoms or nitrogen vacancy [29,30], coupling with other semiconductors or dyes [31,32], controlling morphology [33,34] have been used, and g-C₃N₄-based photocatalysts have shown encouraging activity improvement [22,35,36]. For instance, Han et al reported a mesh-on-mesh network assembled of in situ formed 2D g-C₃N₄ meshes with 2D graphene meshes, g-C₃N₄@graphene hybrid catalysts, via a simple template-free method with excellent hydrogen evolution reaction activity [22]. Zhao et al investigated g-C₃N₄/MoS₂ photocatalysts prepared by a simple and scalable in situ light-assisted method enhancing the H₂ evolution activity because of the MoS₂ cocatalyst for the improvement of the photocatalytic activity of g-C₃N₄ [35]. Hou et al prepared 2D porous g-C₃N₄ nanosheets/nitrogen-doped graphene/layered MoS₂ ternary nanojunction which exhibited good photoelectrochemical and photocatalytic activities under visible light [36].

Recently, it is worth noting that 2D MoS₂/graphene (MG) composite has been adopted as a hybrid cocatalyst which has been introduced to a variety of semiconductor based photocatalysts such as TiO₂ [37,38],

* Corresponding author.

E-mail addresses: tianhw@jlu.edu.cn, wolftian@126.com (H. Tian), wzheng@jlu.edu.cn (W. Zheng).

CdS [39,40], ZnIn₂S₄ [41] and Bi₂WO₆ [42,43]. In previous studies, Xiang et al. reported TiO₂ nanocrystals grown in the presence of a layered MG hybrid by a two-step simple hydrothermal process as a high-performance photocatalyst for H₂ evolution in which MG had higher cocatalytic activities on TiO₂ than pure MoS₂ and graphene [37]. Chang et al. indicated that CdS nanocrystals grown on the surface of a nanosized MG hybrid could be a high-performance noble-metal-free photocatalyst for H₂ evolution under visible light irradiation [40]. In our recent work, we reported an effective strategy to synthesize ternary Bi₂WO₆@MoS₂/graphene photocatalyst by inletsing MoS₂ as a “stepping-stone” into Bi₂WO₆ and graphene, which exhibited superior photocatalytic activity via gradual charge transferred pathway [43]. The layered structure of 2D MG hybrid cocatalyst may have beneficial effect on the catalytic activity. Charge-transfer between MG and main catalyst’s layers are important causes of the superior catalytic activity of the nanocomposites. Moreover, as layered semiconductors, few-layer MoS₂ is an ideal candidate owing to its suitable band-edge positions and good lattice matching with g-C₃N₄, which can enhance light harvesting and promote photogenerated charge separation across the interfaces. Similarly, 2D graphene can be used as an electron mediator for shuttling electrons, leading to effective separation of photogenerated carriers at the junction interface. Thereby, it is expected that higher photocatalytic activities for noble-metal-free catalysts are achieved when MG cocatalyst was supported on junction-matched g-C₃N₄. Moreover, this kind of system can be achieved under visible light, further improving the efficiency of solar energy.

Herein, we report a novel 2D heterojunction g-C₃N₄/MoS₂/graphene (CN/MG) with a 2D heterostructure, g-C₃N₄ in the middle and MG layers at the above and below, via an in-situ adsorption method. CN/MG exhibited superior photocatalytic performance for the degradation of Rhodamine (Rh) B under visible light irradiation compared with g-C₃N₄, g-C₃N₄/MoS₂ (CN/M) and g-C₃N₄/graphene (CN/G), and the degradation rate reached 0.1268 min⁻¹ which is 4.8 times the degradation rate of g-C₃N₄. CN/MG also has favorable stability and photoelectrochemical activities. This kind of 2D layered structural photocatalyst not only can provide abundant reactive sites for photo-degradation but also can increase the transport of charges and reduce the recombination probability of photoexcited charge carriers to obtain enhancement of the photocatalytic activity.

2. Experimental results and discussion

2.1. Materials

Sodium molybdate dihydrate (Na₂MoO₄·2H₂O) was provided from Tianjin Fengchuan Chemical Reagent Company (Tianjin, China). Hydrochloric acid (HCl) were purchased by Beijing Chemical Works (Beijing, China). Thiourea and melamine were purchased by Sinopharm chemical reagent (Shanghai, China). Graphite powder was supplied from Alfa Aesar China (Tianjin, China). All materials were used as received without further purification. Deionized (DI) water used in the preparation was from local sources.

2.2. Synthesis of g-C₃N₄ nanosheets

The g-C₃N₄ nanosheets photocatalyst was obtained through a simple two-step thermal oxidation procedure by using melamine powder as the precursor. The melamine precursor was calcined at 550 °C for 4 h in ambient atmosphere to obtain the bulk C₃N₄ with a ramp rate of 5 °C/min. The resultant yellow agglomerates were milled into powder in a mortar. To increase its specific surface area, the as-prepared bulk C₃N₄ sample was further treated by a calcination method. In briefly, 500 mg of the milled bulk C₃N₄ powder was heated at 500 °C for 2 h with a ramp rate of 5 °C/min. Finally, a light yellow powder of g-C₃N₄ nanosheets was obtained.

2.3. Synthesis of graphene oxide and MG

The graphene oxide (GO) and MG were synthesized according to a procedure described in a previous study [43]. In detail, GO was prepared by a modified Hummers method using natural graphite flakes as the starting material. The MG nanocomposite was synthesized by a one-step hydrothermal reaction of Na₂MoO₄·2H₂O and thiourea in aqueous solution containing exfoliated GO. All of the reagents were of analytical grade and were used without further purification. 135 mg of asprepared GO powders were dispersed into 30 mL of DI water and ultrasonicated until clear yellow-brown suspensions were acquired. After that, a mixture of 1 mmol of Na₂MoO₄·2H₂O and 5 mmol of thiourea was dissolved into the above suspensions and stirred for 30 min. Then the mixture solution was transferred into a 100 mL Teflon-lined stainless steel autoclave, sealed tightly, and heated at an oven at 210 °C for 24 h. After cooled naturally, the black precipitates were gathered by centrifugation, washed with DI water and anhydrous ethanol in sequence, and finally dried at an oven at 80 °C for 12 h to obtain as-prepared MG powder. With the same method as above, different amounts of GO (according to the weight ratio of GO in composite of 0%, 2%, 5%, 8% and 100%, respectively) were added into the starting material solution.

2.4. Synthesis of CN/M, CN/G and CN/MG

The nanocomposites were prepared adopting an in-situ adsorption method. In a typical procedure, 200 mg of asprepared g-C₃N₄ powders were dispersed into 0.1 mol/L HCl solution (pH = 4), then stirred for 30 min at room temperature. A certain quality of MG was added into the above suspensions and stirred for 30 min sequentially. After that, the suspensions were raised the temperature to 90 °C and maintained for 3 h under strongly stirring. After cooled naturally, the precipitates were gathered by centrifugation, washed with DI water for several times, and finally dried at an oven at 60 °C over night to obtain as-prepared CN/MG powder. For comparison, the mechanical mixing of 200 mg of g-C₃N₄, 10 mg MoS₂ and 0.5 mg GO was also prepared under the same experimental conditions, labeled as Mechanical Mixed. With the same method as above, CN/M, CN/G and other samples were also synthesized with adding MoS₂, graphene and different amounts of MG (according to the weight ratio of MG in composite of 1%, 5% and 8%, respectively) were added into the starting material solution.

2.5. Characterization

The X-ray diffraction (XRD) patterns of all samples were taken on a Bruker D8 Advance X-ray diffractometer (Cu K α radiation) in the range of 10–70° with a scan speed of 6° min⁻¹. The Raman spectra was surveyed by laser confocal micro-Raman spectroscopy with an excitation wavelength of 514 nm. The morphologies of photocatalysts were obtained on field emission scanning electron microscopic (FESEM, Hitachi, SU8010). Transmission electron microscopy (TEM) and high-resolution transmission electron microscopy (HRTEM) images were obtained by a JEOL model JEM-2100F instrument operated at 200 kV. All SEM samples were created by depositing a drop of diluted suspensions in ethanol on a silicon chip. All TEM samples were obtained by depositing a drop of diluted suspensions in ethanol on a carbon-film-coated copper grid and naturally dried. Fourier transform infrared spectra (FTIR) was collected using KBr pellets by a Biorad FTS-60A equipped with a diffuse reflectance unit. Ultraviolet-visible (UV-vis) absorption spectra of samples were analyzed by using a spectrophotometer (UV-2500, Shimadzu, Japan), in which BaSO₄ was used as the reference. The chemical composition of photocatalysts was analyzed with X-ray photoelectron spectroscopy (XPS) analysis was conducted using a Thermo ESCALAB 250 spectrometer with a hemisphere detector at an energy resolution of 0.1 eV offered by an Al Ka radiation source. The photoluminescence spectra (PL) was examined with a fluorescence spectrophotometer (F-4600, Hitachi, Japan). The

Brunauer-Emmett-Teller (BET) specific surface areas of the sample powders were obtained through nitrogen adsorption-desorption, measured on an ASAP 2020 micromeritics surface and porosity analyser (USA). The visible light was supplied by a 300 W Xe arc lamp (PL S-SXE 300, Beijing Perfect Light Co., Ltd.) with a cutoff filter ($\lambda > 400$ nm) as the light source.

2.6. The photocatalytic test of the materials

The photocatalytic activity of the photocatalyst was performed by the degradation of Rhodamine (Rh) B and tetracycline (TC), using a 300 W Xe arc lamp equipped with a UV cut off filter ($\lambda > 400$ nm) as the visible light irradiation source. In a typical photocatalytic experiment, 20 mg of photocatalyst was totally dispersed in 60 mL Rh B or TC solution (1.0 mg L⁻¹), and then the suspension was stirred for 30 min in the dark to ensure absorption-desorption equilibrium, after which the reaction suspension was irradiated for 20 min under visible light. At certain time intervals, 4.0 mL of the suspension was withdrawn, and centrifuged to remove the particles, and the concentration of Rh B or TC was analyzed by recording the absorbance using UV-vis spectrophotometer to determine the concentration of Rh B and TC through observing the 554 nm and 356 nm absorption peak, respectively. The degradation ratio was defined as $(C_0 - C)/C_0$, where C referred to the absorption of dye in solution at a certain moment and C_0 referred to the absorption of the initial concentration at each time point.

2.7. Photoelectrochemical performance

The photoelectrochemical analysis was conducted by Transient photocurrent response and Electrochemical impedance spectroscopy (EIS) measurements in a three-electrode system on a CHI650D electrochemical work station. The working electrode was prepared on fluorine-doped tin oxide (FTO) substrate which was cleaned by sonication in ethanol for 30 min and dried at 80 °C. The boundary of FTO glass was protected using scotch tape. 10 mg sample (g-C₃N₄, CN/M, CN/G and CN/MG powders, respectively) was dispersed in 0.1 mL mixed ethanol solution with 10 vol% N,N-Dimethylformamide (DMF) by sonication to get slurry. Then the slurry of sample was deposited onto FTO conducting glass with a working area of 1.0 × 1.0 cm² as the working electrode, which was dried at 100 °C for 2 h in a N₂ atmosphere. At last, the scotch tape was unstuck. Saturated calomel electrode (SCE) and Pt wire were used as the reference electrode, as the counter electrode. The electrolyte was 0.5 M Na₂SO₄ aqueous solution without additive. A 300 W Xe lamp with a 400 nm cut-off filter was used for excitation with external 0.5 V.

2.8. Active species trapping experiments

To determine the active species in the photocatalytic process, some sacrificial agents, such as ethylenediaminetetraacetic acid disodium (EDTA-Na₂), *tert*-butyl alcohol (TBA), and 1,4-benzoquinone (BQ) were used as the hole (h⁺) scavenge, hydroxyl radical (·OH) scavenger, and superoxide radical (·O₂⁻) scavenger, respectively. The method was analogous to the former photocatalytic activity test with the addition of 1 mM of scavenger in the presence of TC after adsorption-desorption equilibrium in dark.

3. Results and discussion

3.1. Synthesis strategy

The two-step synthetic procedure to construct well-contacted 2D CN/MG heterostructure was illustrated in Fig. 1. At first, the deep yellow bulk C₃N₄ sample was obtained through a simple calcination method by using melamine powder as the precursor. Then buff powder of g-C₃N₄ nanosheets was obtained by further thermal oxidation

procedure, which intercalated layers split into fewer layers. The basis of this method is that the hydrogen-bond cohered strands of polymeric melon units in the layers, particularly for short ones, which are not stable enough against or reactive to oxidation process in air, will be gradually oxidized away from the bulk material so that the thickness of bulk C₃N₄ will be decreased to the desired nanoscale [13].

More importantly, when g-C₃N₄ nanosheets was dispersed in acid solution, the protonation brings forth the surface charge modification with positive charged surface [29]. Interestingly, MG that synthesized by the hydrothermal reaction was found to exhibit a negative charged surface. Thus, the oppositely charged g-C₃N₄ nanosheets will be spontaneously assembled on by MG layer with π-π stacking and electrostatic attraction via an in-situ adsorption method. On account of the 2D sheet structure of g-C₃N₄ nanosheets, the MG nanosheets will load on above or below the surface of the g-C₃N₄ nanosheets with intimate interfacial contact. Such interaction will benefit the formation of well-contacted interfaces and consequently facilitate the electron transportation during photoreduction reaction. In this way, the exceptional CN/MG hybrid with an ideal 2D heterostructure was fabricated.

3.2. Structure and morphologies analysis

The crystal structures of as-prepared samples were characterized by XRD. As demonstrated in Fig. 2A, for pure bulk C₃N₄ sample, the characteristic peaks at 13.1° and 27.3° correspond to the (100) plane diffraction arising from the in-plane repeating motifs of the continuous tri-triazine network, and the (002) plane arising from the stacking of the conjugated aromatic system (JCPDS 87-1526), respectively. With respect to the bulk C₃N₄, the peak of g-C₃N₄ originated from the periodic stacking of layers in the nanosheets was shifted from 27.3° to 27.7°, indicating a decreased gallery distance between the basic sheets in the nanosheets. It is found that the main diffraction peaks of CN/M, CN/G and CN/MG nanojunction samples are indexed to be g-C₃N₄ phase. Moreover, all the identified peaks of MoS₂ located at 14.4°, 33.2°, 39.6°, 49.8° and 58.6° corresponding to the (002), (100), (103), (105) and (110) plane are indexed to molybdenite MoS₂ (JCPDS 73-1508). Obviously, the diffraction-peak of MoS₂ phase can be found in CN/M and CN/MG compared with the pure g-C₃N₄ sample, revealing that the cocatalyst MoS₂ and MG has been existed in CN/M and CN/MG, respectively. Significantly, the two characteristic peaks at about 1353 cm⁻¹ (D band) and 1596 cm⁻¹ (G band) for the graphitized structures are observed in the Raman spectrum of the MG composite (Fig. S1). Thus, the Raman spectra of MG and GO can further confirm the presence of graphene in MG.

The chemical structure of the CN/MG nanojunction was further studied by FTIR spectra. As shown in Fig. 2B, the FTIR spectrum of pure g-C₃N₄ nanosheet shows five characteristic bands in the 1200–1700 cm⁻¹ region, which could be assigned to the stretching modes of CN heterocycles (C—N & C=N). Additionally, the typical breathing mode of the triazine units at 816 cm⁻¹ and the stretching vibration mode of N—H at 3235 cm⁻¹ are observed, respectively, indicating the presence of a typical structure of g-C₃N₄. Compared with CN/G, almost all the oxygen-containing functional groups disappear in the FTIR spectrum of the CN/MG nanojunction after the reduction reaction, including C—O stretching vibrations of epoxy groups at 1075 cm⁻¹ and C=O stretching vibrations of COOH groups at 1724 cm⁻¹, indicating the reduction of GO had been occurred. This result can be further confirmed by XPS observations. Notably, in the CN/MG nanojunction, the breathing mode of triazine units at 816 cm⁻¹ exhibits a slight-shift toward a higher wavenumber compared with that of g-C₃N₄, suggesting that the hybridization may occur between g-C₃N₄ and MG sheets [44].

To reveal the valence states and the surface chemical composition of the composite, XPS analysis was performed. In Fig. 3A, elements of C and N are all present in the g-C₃N₄, CN/M, CN/G and CN/MG nanojunction. O element can be seen in CN/G and CN/MG because of GO is

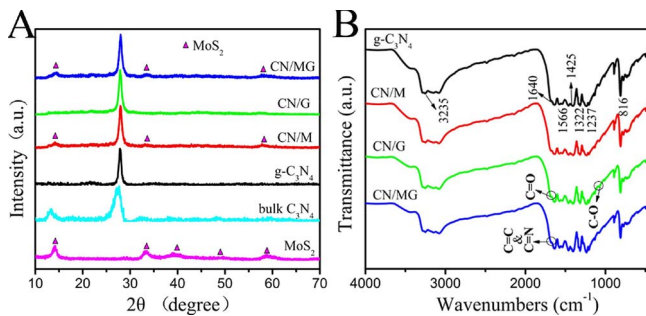
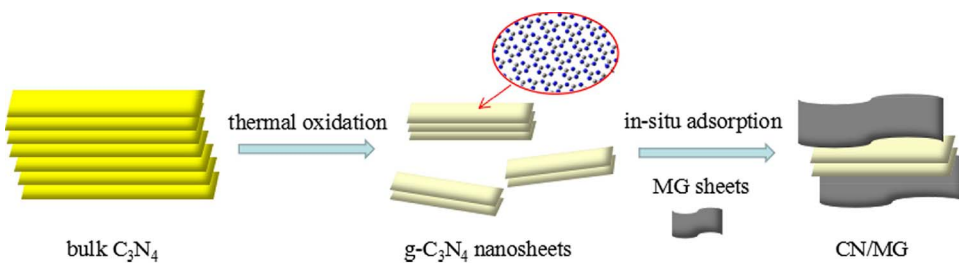


Fig. 2. X-ray diffraction patterns (A) and FTIR spectra (B) of g-C₃N₄, CN/M, CN/G and CN/MG nanojunction.

not completely reduced, indirectly proved the presence of graphene in the CN/MG ternary nanojunction. Moreover, Mo and S elements of CN/M and CN/MG in Fig. 3A has been magnified in Fig. 3B–C. Two peaks for the Mo 3d are observed at 228.8 and 232.0 eV (Fig. 3B), assigned to Mo 3d_{5/2} and Mo 3d_{3/2} in the CN/MG composite, respectively. Compared with CN/MG, these peaks in CN/M are shifted to 228.3 and 231.7 eV, respectively, indicating the presence of a strong interaction between MG and g-C₃N₄. In addition, note that a similar result is obtained for the binding energies of S 2p_{3/2} and S 2p_{1/2}. XPS peaks of S 2p located at 161.5 and 162.9 eV can be assigned to the spectra of S 2p_{3/2} and S 2p_{1/2} for CN/MG (Fig. 3C), which is in accordance with the sulfur element in the sulfides. It is observed that the peaks of S 2p_{3/2} and S 2p_{1/2} in CN/M are shifted slightly up by 0.3 and 0.2 eV (Fig. 3C), respectively, suggesting chemical bonding may be present between g-C₃N₄ and MG.

The corresponding high-resolution N 1s spectrum of the

nanojunction can be deconvoluted into five peaks centered at 397.9, 398.8, 399.5, 401.3, and 404.3 eV, corresponding to N-graphene, pyridine N, pyrrolic N, graphitic N, and N-O' (oxidized nitrogen), respectively (Fig. 3D). The N-graphene peak may be attributed to the nitrogen bonding between g-C₃N₄ and graphene, which can serve as a bridge linking g-C₃N₄ with MG [36]. The high-resolution C 1s spectrum of CN/MG displays five fitted peaks at 284.5, 284.9, 285.4, 288.3, and 289.3 eV, which are assigned to the C–C, C–OH, C–O–C, C–N, and O–C=O configurations, respectively (Fig. 3E). Compared with the C 1s spectrum of GO (Fig. 3F), the constituents of oxygen functionalities decrease after g-C₃N₄ being modified by MG observed in CN/MG (Fig. 3E), suggesting moderate reduction of GO to RGO and the presence of graphene in the ternary nanojunction. In Fig. 3E, a new peak at 288.3 eV attributed to the C–N bond instead of C=O bond is considered as the major carbon species in g-C₃N₄ (Fig. S2). Obviously, the amount of oxygen-functional groups has diminished greatly after modified by MG, indicating that most oxygenate groups has been efficiently removed, which is beneficial to the charge separation between g-C₃N₄ nanosheets and layered MG.

The microstructures of the g-C₃N₄, MG and the CN/MG were examined by SEM, TEM and HRTEM, respectively. The SEM image (Fig. S3A) and TEM image (Fig. 4A) of the g-C₃N₄ show thin and irregular nanosheet structure, which indicate the obtained g-C₃N₄ is consisted of monolayers or few atomic layers. Graphene can be clearly observed in the binary MG cocatalyst, as shown in Fig. 4B. MG composite has a layered structure with interlayer spacing of ca. 0.62 nm which corresponds to the (002) planes of MoS₂ (Fig. S4). The MG nanosheets were horizontal loaded on above or below the surface of the g-C₃N₄ nanosheets with intimate interfacial contact, which can be seen in Fig. 4C with a part of the stagger layers stacking structure. An HRTEM image of

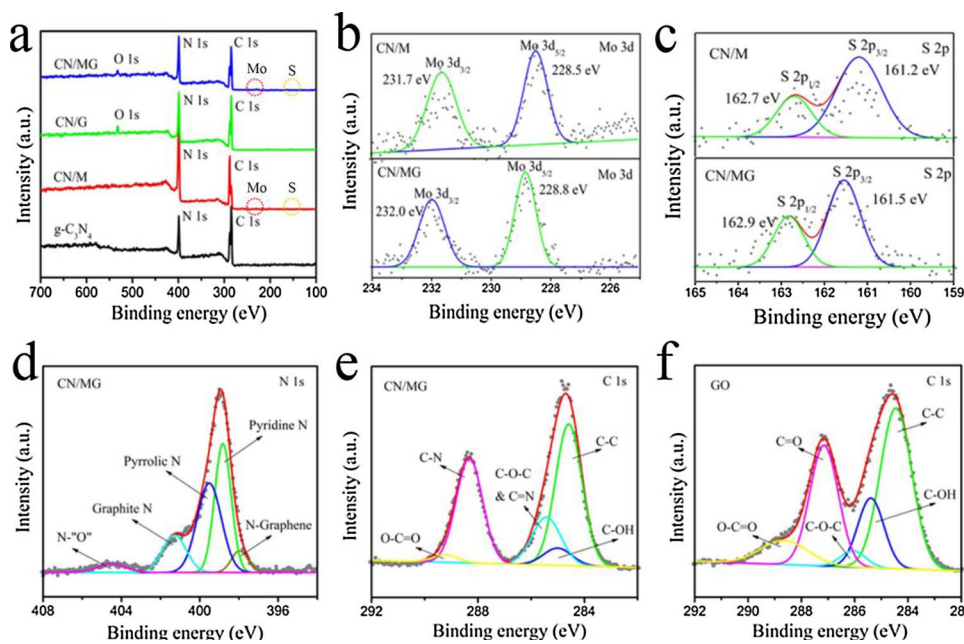


Fig. 3. The overall XPS spectrum (A) for the g-C₃N₄, CN/M, CN/G and CN/MG nanojunction. Mo 3d (B), S 2p (C), N 1 s (D) and C 1 s (E) XPS spectra for the CN/MG nanojunction. The Mo 3d and S 2p XPS spectra of CN/M were added into (B, C) for comparison. C 1 s XPS spectra for the GO (F).

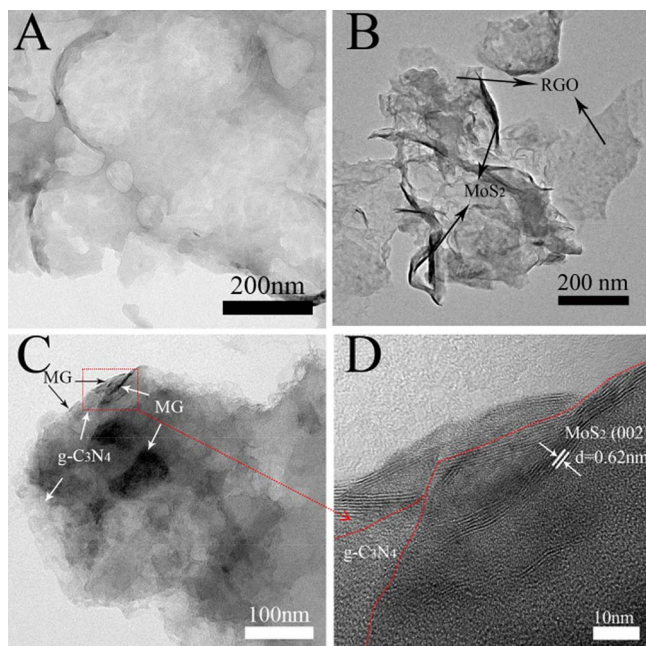


Fig. 4. TEM images of g-C₃N₄ (A), MG (B) and CN/MG (C); HRTEM image (D) of CN/MG.

CN/MG shows that the numbers of MoS₂ layers in MG is approximately 2–8 with lattice spacing of 0.62 nm (Fig. 4D), which illustrates MG still remains excellent nanoscale layered structure after coating on 2D g-C₃N₄ nanosheets. Furthermore, based on the selected region in Fig. S3B, the corresponding elemental mapping analysis clearly showed the well-defined spatial distribution of all elements C, N, Mo, and S in Fig. S3C–F, confirming the formation of the CN/MG nanojunction with an intimate contact between g-C₃N₄ nanosheets and layered MG. It is worth mentioning that the 2D structure of CN/MG could effectively increase the contact area, which could result in better separation of photoinduced charge carriers and more efficient electron transfer within the composite structure.

3.3. Photocatalytic and photoelectrochemical performance

The photocatalytic activity of as-prepared samples was evaluated using Rh B degradation as shown in Fig. 5A. Additionally, to make comparison, mechanical mixture of g-C₃N₄, MoS₂ and graphene samples were also taken into consideration in this reaction system. In binary material, as shown in Fig. S5, we chose 95MoS₂/5graphene (MG, the optimum dopant graphene weight is 5 wt%) as the control to prepare photocatalytic activity to a certain extent and CN/MG presents. Moreover, a series of the CN/MG composites with different amounts of hybrid cocatalyst (denoted as 99CN/1MG, 95CN/5MG and 92CN/8MG) were prepared and the ternary heterojunction of 5% MG hybrid and 95% g-C₃N₄ showed the highest photodegradation rate (Table S1). As shown in Fig. 5A, the CN/MG ternary composites exhibit an excellent photocatalytic activity better than the pure g-C₃N₄, CN/M, CN/G and mechanical mixed sample. Before illumination, the suspensions were stirred in dark for 30 min to reach the adsorption-desorption equilibrium. When the illumination time is 20 min, the degradation rate of CN/MG reached 95%, the prominently highest photoactivity, and the apparent reaction rate constant of the ternary material in Fig. 5B is 0.1268 min⁻¹, which is almost 4.8 times the degradation rate of g-C₃N₄. It displays the concentration changes of Rh B at 554 nm as a function of irradiation time during the degradation process in aqueous CN/MG in Fig. 5C. The change of TOC concentration reflected the mineralization degree of Rh B dye in Fig. S6. The ternary CN/MG catalyst shows higher TOC removal rate of Rh B compared with g-C₃N₄, which basically coincides with the result of the degradation rate. The

TOC removal contents of g-C₃N₄ and CN/MG are 23.53% and 41.63% under the visible light irradiation for 20 min. This phenomenon suggests that Rh B molecules are most likely mineralized into some intermediate and inorganic molecules. Fig. 5D presents that the degradation efficiency shows a slight decrease after three recycling runs, which directly certify the stability of CN/MG in the Rh B photodegradation process. We believe that excellent photocatalytic performance of CN/MG ternary composite thanks to MG cocatalyst which provides larger specific surface area, more photocatalytic reaction centers and faster electron transfer pathway.

In terms of the stability of crystal structure and chemical structure of the CN/MG nanojunction, the XRD and FTIR spectra of CN/MG after three cycle times (CN/MG-Cycle) were further studied. XRD spectra of CN/MG-Cycle is shown in Fig. 6A. Compared to original CN/MG, it can be seen that the diffraction peaks of CN/MG-Cycle are similar to that of CN/MG, revealing that the catalyst CN/MG has good stability for crystal structure. As shown in Fig. 6B, the FTIR spectra of the CN/MG-Cycle nanocomposites nearly stay the same as that of CN/MG samples. The results demonstrated the excellent stability of the prepared CN/MG hybrid photocatalysts.

The photocatalytic activities of the as-prepared samples were further studied by the degradation of TC under visible light irradiation for evaluating the photocatalytic activity of materials and eliminating the indirect dye photosensitization in the photocatalytic system. As shown in Fig. 7, TC was hardly degraded without catalyst under visible light irradiation. And CN/MG had the most excellent photocatalytic activity for photocatalytic degradation of TC with different photocatalysts under visible light irradiation. Furthermore, the TC degradation rate of Mechanical Mixed sample, g-C₃N₄, MoS₂ and graphene mechanical mixed, reached ~54% under 20 min visible light irradiation which was still much lower than that of CN/MG (~69%). It may suggest that Mechanical Mixed sample didn't have well-contacted interface and fast charge transfer pathway.

The photoelectrochemistry activity of the samples were measured by means of the transient photocurrents during repeated ON/OFF illumination cycles. All of the samples exhibit prompt and reproducible photocurrent responses on each illumination (Fig. 8A). When the irradiation was interrupted, the photocurrent rapidly dropped to steady-state value, and the photocurrent reverted to the original value once light was switched back on again. As shown in Fig. 8A, the photocurrent density of the CN/M is higher than that of the g-C₃N₄, which can be attributed to MoS₂ nanosheets trapping electrons. The transient photocurrent density of the CN/G is also more than that of the g-C₃N₄. This result confirms the constructive effect of the graphene in promoting electron shuttling and suppressing charge recombination, where graphene acted as an electron transfer channel, transferring the photo-generated electrons from g-C₃N₄. Moreover, note that the CN/MG nanojunction exhibited the highest transient photocurrent density among the samples tested. This enhancement of photocurrent density probably resulted from the enhanced light harvesting owing to the loading of MoS₂ nanosheets and more efficient separation of photogenerated electro-hole pairs owing to the formation of graphene-based ternary layered heterojunctions.

To gain deeper insights into the charge transport behavior in the nanojunction system, we conducted EIS measurements (Fig. 8B). In the Nyquist diagram, the radius of each arc is associated with the charge-transfer process at the corresponding electrode/electrolyte interface with a smaller radius corresponding with a lower charge-transfer resistance. The CN/MG nanojunction exhibits the smallest charge transfer resistance among all g-C₃N₄-based electrodes under irradiation, suggesting that effective shuttling of charges between the electrode and the electrolyte, and faster interfacial charge transfer occurred at the composite interface owing to the formation of the nanojunction.

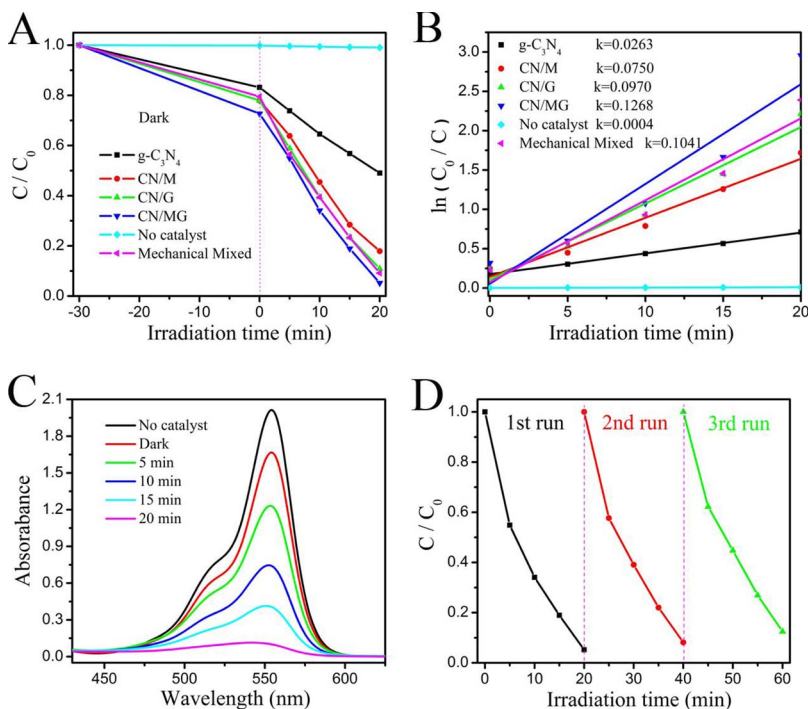


Fig. 5. Photocatalytic degradation of Rh B (A) and the photodegradation plots with the apparent reaction rate constants k for the photodegradation of Rh B (B) of $\text{g-C}_3\text{N}_4$, CN/M, CN/G, CN/MG nanojunctions and mechanical mixed sample under visible light ($\lambda > 400 \text{ nm}$); absorption changes of Rh B solution (10 mg/L, 60 mL) containing 20 mg CN/MG powders under visible-light-induced photocatalytic process (C); the recycling runs of CN/MG for degrading Rh B (D).

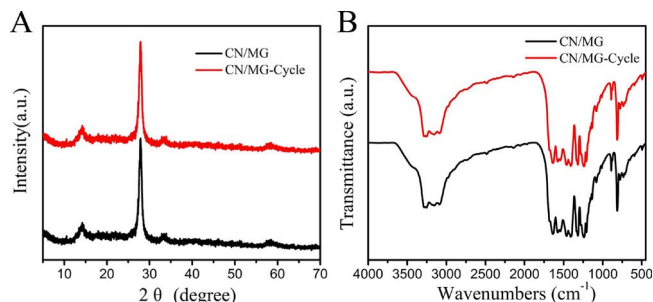


Fig. 6. XRD (A) and FTIR (B) spectra of CN/MG after three cycle times.

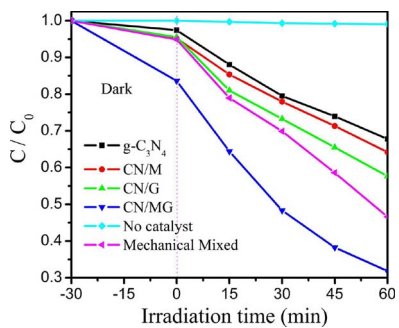


Fig. 7. Photocatalytic degradation of TC of $\text{g-C}_3\text{N}_4$, CN/M, CN/G, CN/MG nanojunctions and mechanical mixed sample under visible light irradiation.

3.4. Mechanism on enhancement of photocatalytic activity

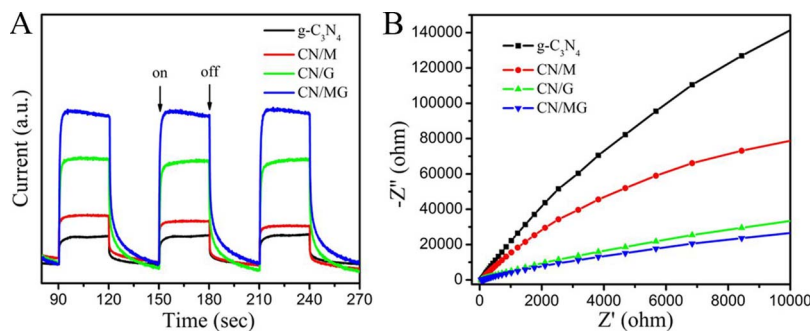
The optical absorption properties play a critical role in determining the photocatalytic performance, especially for the visible-light-driven photocatalysis. The optical properties of the samples were studied by UV-vis absorption spectroscopy in Fig. 9A–B. It can be found that the pure $\text{g-C}_3\text{N}_4$ has an absorption edge at about 448 nm, corresponding to a band gap at 2.84 eV. After the loading of MoS_2 or graphene, sample shows a similar absorption edge with slightly enhanced absorption to the visible region. Once both the MoS_2 and graphene were introduced, the absorption edge of CN/MG samples at 526 nm (corresponding to a

band gap at 2.43 eV) has a red shift by 0.39 eV compared to that of the pure $\text{g-C}_3\text{N}_4$. Namely, the light absorption of the CN/MG composite significantly moves in the visible light range particularly after MG cocatalyst modification, indicating that the loading of MG further improves the light absorption ability of the composite owing to its narrower band gap. The results suggest that the ternary nanojunction may be able to absorb more light to produce electron-hole pairs and thus exhibit improved catalytic activity.

The nitrogen adsorption-desorption isotherms of as-prepared samples exhibit stepwise adsorption behavior as shown in Fig. 9C. The isotherms of $\text{g-C}_3\text{N}_4$ and CN/M display a type IV isotherm with a H4 hysteresis loop, indicating the existence of little micropore stemming from nanoparticles. The isotherms of CN/G and CN/MG reveal a type IV isotherm with a H3 hysteresis loop, suggesting the slit-shaped pores produced by the layered structure. The BET specific surface area (S_{BET}) of $\text{g-C}_3\text{N}_4$, CN/M, CN/G and CN/MG are determined to be $101.002 \text{ m}^2 \text{ g}^{-1}$, $88.987 \text{ m}^2 \text{ g}^{-1}$, $82.658 \text{ m}^2 \text{ g}^{-1}$ and $99.997 \text{ m}^2 \text{ g}^{-1}$, respectively. Although the subsequent introduction of MG sheet decreases the total surface area, there still remains a high specific surface area of $99.997 \text{ m}^2 \text{ g}^{-1}$ for the CN/MG nanojunction. The pore size analysis shows that the average pore size of all samples is $\sim 3.0 \text{ nm}$ (Fig. 9D) attributed to the coupling of $\text{g-C}_3\text{N}_4$ and different cocatalyst with excellent interface contact in the 2D structure. With a large surface area, the CN/MG nanojunction might hold great promise in offering sufficient interfacial area for more active adsorption or catalytic sites.

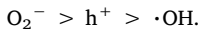
The migration of photo-generated electron-hole pairs in our samples was investigated by PL analysis with an excitation wavelength of 380 nm. As shown in Fig. S7, it can be found that a strong PL emission peak of all samples is observed at about 445 nm, which can be attributed to the recombination of photo-induced electrons and holes for $\text{g-C}_3\text{N}_4$. Moreover, the emission-peak intensity of the CN/M, CN/G and CN/MG photocatalyst gradually decrease with different cocatalyst modification of MoS_2 , graphene or MG, indicating a lower recombination possibility of photogenerated charge carriers than $\text{g-C}_3\text{N}_4$. This phenomenon is attributed to the efficient charge transfer between $\text{g-C}_3\text{N}_4$ and MG interlayer, which prevents the direct recombination of electrons and holes.

In order to further confirm the energy band structures photocatalysts, the density of states (DOS) of the valence band (VB) in VB XPS



spectra and schematic illustration was obtained as shown in Fig. 10. The DOS of the VB is presented in Fig. 10A–E. The VB DOS with the edge of the maximum energy for g-C₃N₄, CN/M, CN/G, CN/MG and MoS₂ are displayed at about 1.45 eV, 1.50 eV, 1.44 eV, 1.49 eV and 1.52 eV, respectively. According to the band gap of the photocatalysis (as shown in UV-vis absorption spectra above) [45], the conduction band (CB) minimum of g-C₃N₄, CN/M, CN/G, CN/MG and MoS₂ would present at about −1.39 eV, −1.22 eV, −1.17 eV, −0.94 eV and −0.26 eV by calculation, respectively. From the schematic illustration of the DOS of these samples (Fig. 10F), the CBs of g-C₃N₄ have been effectively adjusted after different cocatalyst modification, which was conducive to obtain enhanced photocatalytic performance.

The species trapping experiments for degradation of Rh B over CN/MG photocatalysts under visible light irradiation was shown in Fig. 11 to well investigate and confirm the photocatalytic mechanism. When the EDTA-Na and BQ are used, the photodegradation rates of Rh B are distinctly reduction, and are ~49% and ~20%, respectively, which indicates h⁺ and ·O₂[−] are main activated species. On the contrary, it can be found that the photodegradation rate of Rh B still reaches to ~85% in the presence of TBA, which is slightly lower than that of without any trapping agents (~95%). It implies that ·OH has almost a little effect on photodegradation of Rh B. Thus, in the process of Rh B photodegradation, the influence order of the activated species is ·



Based on the above results and analysis, MG modification gives a top priority to enhance g-C₃N₄ nanosheets' photocatalytic activity in ternary nanocomposites. As shown in Fig. 12, we propose a possible photocatalytic mechanism for the CN/MG photocatalyst under visible light irradiation. It's worth noting that in the presence of visible light both MoS₂ and g-C₃N₄ can be simultaneously excited to generate electron-hole pairs. The photoexcited electrons (e[−]) in the VB of g-C₃N₄ and MoS₂ would easily transfer into the CB leaving h⁺ in the VB. Additionally, the Rh B molecules can also be photoexcited under visible light irradiation [46]. Because the E_{CB} of g-C₃N₄ (-1.39 V vs. NHE) is more negative than that of MoS₂ (-0.26 V vs. NHE), the photoexcited electrons would transport from the CB of g-C₃N₄ to the CB of MoS₂, then to RGO with strong reductive ability which can react with the dissolved oxygen molecule (O₂) to obtain ·O₂[−]. Meanwhile, the photoexcited holes on the VB of MoS₂ can transfer to the VB of g-C₃N₄ according to the energy band structure. Meaningfully, MoS₂ and graphene can capture these photoexcited electrons and quicken the mobility hindering the recombination of photogenerated electron-hole pairs. These present electrons and holes of g-C₃N₄ and MoS₂ can react with the adsorbed molecules directly to produce many strong oxidants including ·OH and ·O₂[−] radicals. These oxidative species play crucial roles in the oxidative degradation of organics. In the end, the CN/MG hybrid destroys the

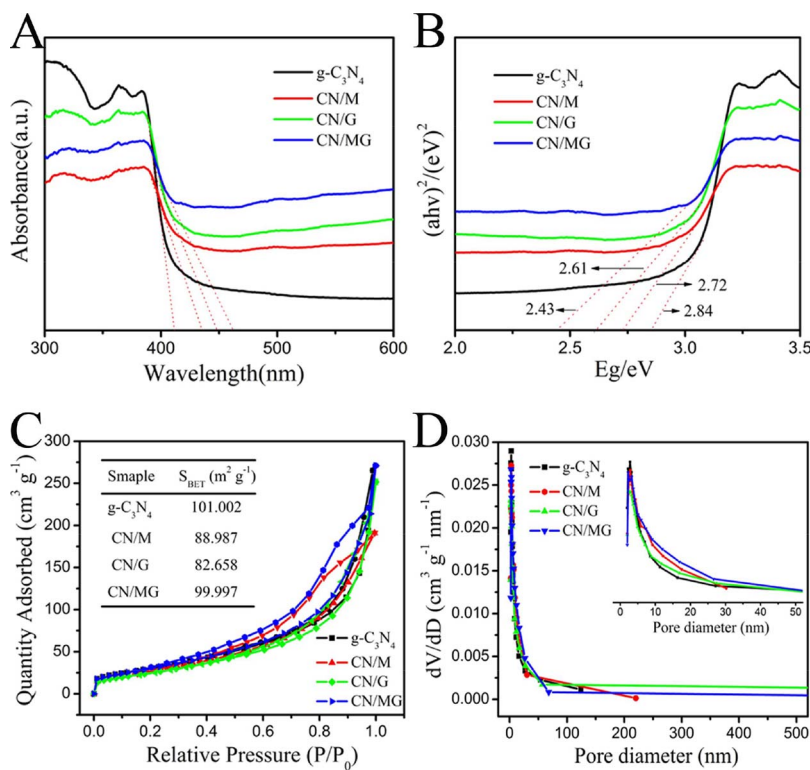


Fig. 9. UV-vis absorption spectra (A), the corresponding Kubelka-Munk function (B), Nitrogen adsorption-desorption isotherm (C) and the corresponding pore size distribution curves calculated from adsorption branch of the nitrogen isotherm (D) of g-C₃N₄, CN/M, CN/G and CN/MG photocatalysts.

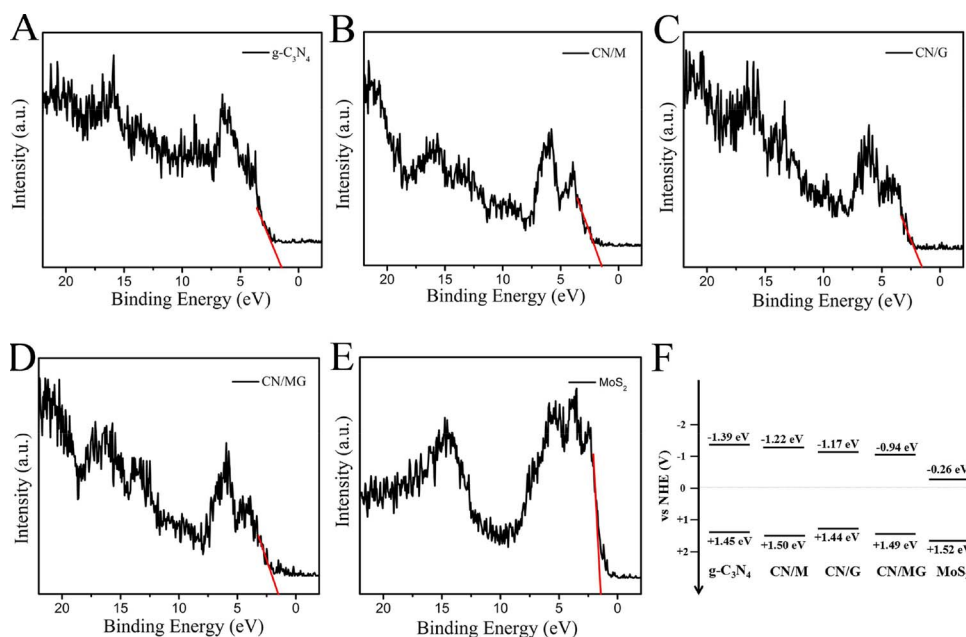


Fig. 10. VB XPS spectra of $\text{g-C}_3\text{N}_4$ (A), CN/M (B), CN/G (C), CN/MG (D) and MoS_2 (E) photocatalysts. Schematic illustration of the DOS of the photocatalysts (F).

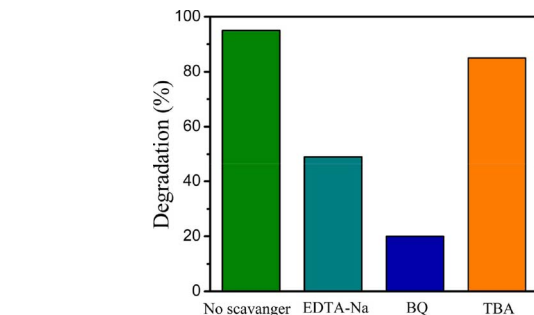


Fig. 11. The species trapping experiments for degradation of Rh B over CN/MG photocatalysts under visible light irradiation.

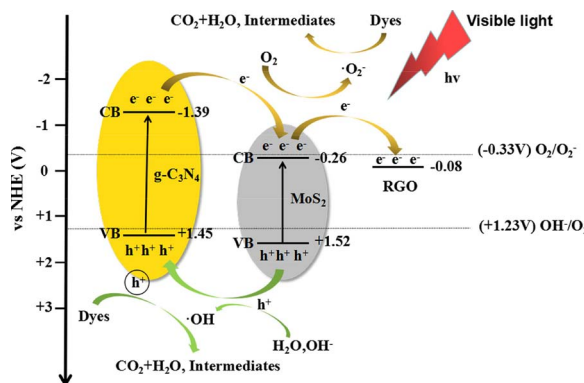


Fig. 12. The possible photocatalytic mechanism for the CN/MG photocatalyst under visible light irradiation.

dye molecules into little pieces, CO_2 , H_2O and other intermediates.

On account of the fast charge transferred pathway, in CN/MG ternary hybrid the photogenerated charge recombination could be effectively suppressed, which effectively prolonged the lifetime of the charge carriers, enlarged the reaction space, and consequently enhanced the photocatalytic activity for photodegradation. Notably, MG cocatalyst led to a significant contribution with several advantages, including suppression of charge recombination, improvement of interfacial charge transfer, and an increasing active adsorption sites' number, specific surface area and photocatalytic reaction centers. The

experimental results discussed in this work demonstrates that an effective designed method to fabricate CN/MG ternary photocatalysts with MG binary cocatalysts as a valuable indication for further development of related $\text{g-C}_3\text{N}_4$ -based photocatalysts composite materials.

4. Conclusions

In summary, a novel 2D CN/MG ternary photocatalyst was designed by an in-situ adsorption method with an enhanced charge carrier separation via fast charge transfer pathway, which shows highest photodegradation activity with a high rate which is almost 4.8 times degradation rate of pure $\text{g-C}_3\text{N}_4$ for the degradation of Rh B under visible light irradiation. Furthermore, superior photoelectrochemical activity and stability were exhibited in the ternary nanocomposite. In CN/MG ternary photocatalyst, MG cocatalyst played a key role on account of the 2D layered structure, which benefits the formation of well-contacted interfaces with $\text{g-C}_3\text{N}_4$ nanosheets and consequently facilitate the electron transportation during photoreduction reaction. The present 2D heterostructure and effective CN/MG photocatalyst may bring new insights into further development of related $\text{g-C}_3\text{N}_4$ -based photocatalyst to be applied in water pollution treatment.

Conflicts of interest

There are no conflicts to declare.

Acknowledgements

Financial support from the National Natural Science Foundation of China (Nos. 51472106 and 51372095), the Natural Science Foundation of Jilin Province and the Key Project of Science and Technology of The Jilin Provincial Education Department during the 13th Five-Year Plan Period are highly appreciated.

Appendix A. Supplementary data

Supplementary data associated with this article can be found, in the online version, at <https://doi.org/10.1016/j.apcatb.2017.12.019>.

References

- [1] W.J. Ong, L.L. Tan, Y.H. Ng, S.T. Yong, S.P. Chai, *Chem. Rev.* 116 (2016) 7159–7329.
- [2] X. Dong, F. Cheng, *J. Mater. Chem. A* 3 (2015) 23642–23652.
- [3] A. Gupta, T. Sakthivel, S. Seal, *Prog. Mater. Sci.* 73 (2015) 44–126.
- [4] H.W. Tian, K. Shen, X.Y. Hu, L. Qiao, W.T. Zheng, *J. Alloy. Compd.* 691 (2017) 369–377.
- [5] B. Luo, G. Liu, L. Wang, *Nanoscale* 8 (2016) 6904–6920.
- [6] M.Z. Rahman, C.W. Kwong, K. Davey, S.Z. Qiao, *Energy Environ. Sci.* 9 (2016) 709–728.
- [7] J. Di, J. Xia, H. Li, Z. Liu, *Nano Energy* 35 (2017) 79–91.
- [8] Q. Xiang, J. Yu, M. Jaroniec, *Chem. Soc. Rev.* 41 (2012) 782–796.
- [9] F. Perreault, A. Fonseca de Faria, M. Elimelech, *Chem. Soc. Rev.* 44 (2015) 5861–5896.
- [10] S. Yang, Y. Gong, J. Zhang, L. Zhan, L. Ma, P.M. Ajayan, *Adv. Mater.* 25 (2013) 2452–2456.
- [11] P.K. Kannan, D.J. Late, H. Morgan, C.S. Rout, *Nanoscale* 7 (2015) 13293–13312.
- [12] C. Tan, H. Zhang, *Chem. Soc. Rev.* 44 (2015) 2713–2731.
- [13] P. Niu, L. Zhang, G. Liu, H.M. Cheng, *Adv. Funct. Mater.* 22 (2012) 4763–4770.
- [14] J. Hao, G. Song, T. Liu, X. Yi, K. Yang, L. Cheng, Z. Liu, *Adv. Sci.* 4 (2017) 1600160.
- [15] M.A. Bissett, S.D. Worrall, I.A. Kinloch, R.A.W. Dryfe, *Electrochim. Acta* 201 (2016) 30–37.
- [16] Y. Zheng, L.H. Lin, B. Wang, X.C. Wang, *Angew. Chem. Int. Ed.* 54 (2015) 12868–12884.
- [17] J. Xu, L. Zhang, R. Shi, Y. Zhu, *J. Mater. Chem. A* 1 (2013) 14766.
- [18] X. Wang, M. Hong, F. Zhang, Z. Zhuang, Y. Yu, *ACS Sustain. Chem. Eng.* 4 (2016) 4055–4063.
- [19] W.C. Peng, X.Y. Li, *Catal. Commun.* 49 (2014) 63–67.
- [20] W. Zhang, X. Xiao, Y. Li, X. Zeng, L. Zheng, C. Wan, *Appl. Surf. Sci.* 389 (2016) 496–506.
- [21] H. Yu, P. Xiao, P. Wang, J. Yu, *Appl. Catal. B: Environ.* 193 (2016) 217–225.
- [22] Q. Han, Z. Cheng, J. Gao, Y. Zhao, Z. Zhang, L. Dai, L. Qu, *Adv. Funct. Mater.* 27 (2017) 1606352.
- [23] M. Li, L. Zhang, X. Fan, Y. Zhou, M. Wu, J. Shi, *J. Mater. Chem. A* 3 (2015) 5189–5196.
- [24] M.Q. Wen, T. Xiong, Z.G. Zang, W. Wei, X.S. Tang, F. Dong, *Opt. Express* 24 (2016) 10205–10212.
- [25] J. Yu, S. Wang, J. Low, W. Xiao, *Phys. Chem. Chem. Phys.* 15 (2013) 16883–16890.
- [26] Y. Dong, Q. Wang, H. Wu, Y. Chen, C.H. Lu, Y. Chi, H.H. Yang, *Small* 12 (2016) 5376–5393.
- [27] X. Zhang, X. Xie, H. Wang, J. Zhang, B. Pan, Y. Xie, *J. Am. Chem. Soc.* 135 (2013) 18–21.
- [28] J. Zhang, Y. Chen, X. Wang, *Energy Environ. Sci.* 8 (2015) 3092–3108.
- [29] J. Chen, X. Xu, T. Li, K. Pandiselvi, J. Wang, *Sci. Rep.* 6 (2016) 37318.
- [30] Q. Liu, T. Chen, Y. Guo, Z. Zhang, X. Fang, *Appl. Catal. B: Environ.* 193 (2016) 248–258.
- [31] W.K. Jo, J.Y. Lee, N.C.S. Selvam, *Chem. Eng. J.* 289 (2016) 306–318.
- [32] Y. Wang, X. Bai, C. Pan, J. He, Y. Zhu, *J. Mater. Chem.* 22 (2012) 11568.
- [33] D. Zheng, G. Zhang, Y. Hou, X. Wang, *Appl. Catal. A: Gen.* 521 (2016) 2–8.
- [34] Q. Gu, H. Sun, Z. Xie, Z. Gao, C. Xue, *Appl. Surf. Sci.* 396 (2017) 1808–1815.
- [35] H. Zhao, Y. Dong, P. Jiang, H. Miao, G. Wang, J. Zhang, *J. Mater. Chem. A* 3 (2015) 7375–7381.
- [36] Y. Hou, Z. Wen, S. Cui, X. Guo, J. Chen, *Adv. Mater.* 25 (2013) 6291–6297.
- [37] Q. Xiang, J. Yu, M. Jaroniec, *J. Am. Chem. Soc.* 134 (2012) 6575–6578.
- [38] D.B. Nimbalkar, H.H. Lo, P.V.R.K. Ramacharyulu, S.C. Ke, *RSC Adv.* 6 (2016) 31661–31667.
- [39] M.Q. Yang, C. Han, Y.J. Xu, *J. Phys. Chem. C* 119 (2015) 27234–27246.
- [40] Z.M.K. Chang, T. Wang, Q. Kang, S.X. Ouyang, J.H. Ye, *ACS Nano* 8 (2014) 7078–7087.
- [41] Y.J. Yuan, J.R. Tu, Z.J. Ye, D.Q. Chen, B. Hu, Z.G. Zou, *Appl. Catal. B: Environ.* 188 (2016) 13–22.
- [42] C. Zhang, G. Chen, C. Li, J. Sun, C. Lv, W. Xing, *ACS Sustain. Chem. Eng.* 4 (2016) 5936–5942.
- [43] M. Liu, X. Xue, S. Yu, X. Wang, X. Hu, H.W. Tian, H. Chen, W. Zheng, *Sci. Rep.* 7 (2017) 3637.
- [44] J. Li, E. Liu, Y. Ma, X. Hu, J. Wan, L. Sun, J. Fan, *Appl. Surf. Sci.* 364 (2016) 694–702.
- [45] K. Shen, X. Xue, X. Wang, X. Hu, H. Tian, W. Zheng, *RSC Adv.* 7 (2017) 23319–23327.
- [46] Q. Quan, X. Lin, N. Zhang, Y.J. Xu, *Nanoscale* 9 (2017) 2398–2416.